Scientia Iranica A (2013) 20(6), 1662–1675

SCIENTIA IRANICA

Sharif University of Technology
Scientia Iranica
Transactions A: Civil Engineering
www.scientiairanica.com

Investigating pore network models as numerical tools to solve steady saturated groundwater flow

P. Monajemi* **and Gh. Rakhshandehroo**

Department of Civil and Environmental Engineering, School of Engineering, Shiraz University, Shiraz, Iran.

Received 28 September 2012; received in revised form 15 April 2013; accepted 22 May 2013

KEYWORDS
Groundwater;
Numerical methods;
Pore network model.

Abstract. In this paper, a novel procedure is introduced and employed to transform the partial differential steady saturated flow equation in porous media into a system of linear equations using Pore Network Models (PNMs). At first, a simple Square Pore Network Model (SPNM) is introduced and then this model is improved by increasing node connectivity (Square-Diagonal PNM; S-DPNM) and modifying the handling of impermeable boundaries by introducing imaginary nodes and pipes (S-DPNMi). Finally, a generalized formulation for the unstructured discretization (Unstructured PNM; UPNM) of the domain is given and the effect of handling impermeable boundaries (UPNMi) on model accuracy is investigated. To explore the capabilities of these models as numerical tools, three examples are solved. Application of these models without modifications for impermeable boundaries (SPNM, S-DPNM, and UPNM) yields comparable results to those of traditional Finite Difference (FD) and Finite Element (FE) methods. Modification in handling impermeable boundary nodes not only yields results that are everywhere more accurate than FD and FE, but also benefits by the simplicity of formulations.

1. Introduction

Pore Network Models (PNMs) are much more systematic than real pore spaces, and hence, have been widely used and developed by many researchers since their first introduction by Fatt in 1956. Complexity of fluid flow in porous media, difficulty in determination of fluid phase relative permeabilities and capillary pressures [1], and an inability to obtain pore scale observations [2] are among reasons that encourage researchers to use PNMs to study fluid(s) flow in porous media.

Investigation of interfacial area, capillary pressure, saturation relationships [3-7], porosity and permeability [8-10], displacement of water by DNAPL [11], and transport properties [3,12] were all done utilizing PNMs. PNMs may be divided into two categories: (1) a network that is only made up of throats and (2) a network that is made up of throats and pores. Throats and pores of PNMs may have different shapes and properties. For example, prismatic throats with circular cross sections were used by Fatt [13], Koplic [14], Mazaheri et al. [15], Joekar-Niasar et al. [7], and Nsir and Schafer [11], while rectangular, triangular, and grain boundary cross sections were considered by Ioannidis and Chatzis [3], Øren et al. [16], Man and Jing [4], Kagen and Pinczewski [17], Joekar-Niasar et al. [5]. Non prismatic throats, mainly converging-diverging types, were used by Dias and Payatakes [18], Thahivan and Mohanty [8], Acharya et al. [10]. Randomly sized pore bodies and throats were utilized by Dias and Payatakes [18], Steele and Nieber [12], Acharaya et al. [10], Pirri and Blunt [1], and Nsir

*. *Corresponding author. Tel.: 0711-6287505; Fax: 0711-6473161*
E-mail addresses: parjang@gmail.com (P. Monajemi), rakhshan@shirazu.ac.ir (Gh. Rakhshandehroo)

and Schafer [11], and a distribution of coordination numbers was considered in the study by Raoof and Hassanizadeh [19].

In this paper, a simple PNM is presented and utilized as a numerical tool with superior capabilities to solve steady saturated flow in porous media. In this model, a porous media is replaced by a network of pipes, which is shown to be governed by the Laplace equation. A simple flexible procedure is then introduced to transform the equation into a set of n-linear algebraic equations. First, a simple example is solved by the model, and then alterations are made on the model to account for node connectivity and boundary condition treatment. Results of these models are verified by their comparison with the analytical solution and their errors are compared with those of Finite Difference (FD) and Finite Element (FE). The sensitivity of models to mesh size is also investigated. Finally, a more complex example is solved by an unstructured PNM to show the capabilities and strengths of the model over FD and FE methods.

2. Methodology and formulation

2.1. Network pattern

It is assumed that a pore network in a porous media may be modeled by elemental tubes forming a network simply consisting of horizontal and vertical cylindrical throats (pipes). No volume is assigned to nodes where the pipes intersect. A typical rectangular PNM is shown in Figure 1. The model architecture is later altered by adding diagonal cylindrical throats. It is worth noting that the cross sectional area and length of the throats would vary where porous media exhibits non-homogeneity and/or an isotropy.

2.2. Discretized flow equation for a typical PNM

A fundamental element for a typical PNM is shown in Figure 2. To develop flow equation for the element, it

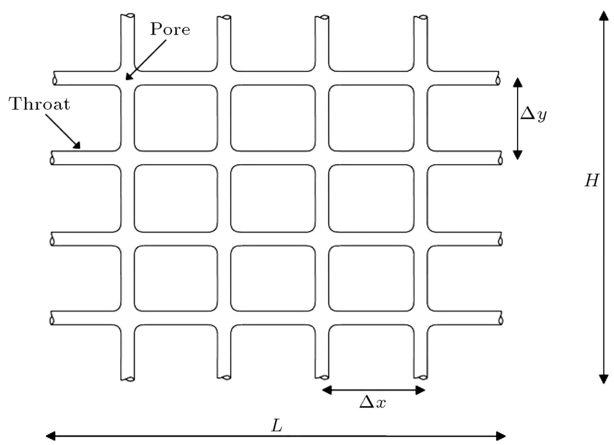

Figure 1. A typical rectangular PNM.

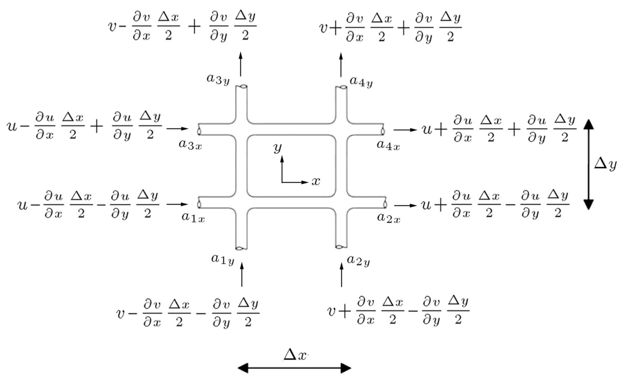

Figure 2. Fundamental element for the typical PNM.

is assumed that:

1. The fluid is Newtonian incompressible.
2. The flow is steady laminar.
3. No capillary pressure exists.

The mass balance equation for the element with 4 inlets and 4 outlets may be written as:

$$Q_{\text{in}} = Q_{\text{out}}, \tag{1}$$

$$\begin{aligned}
&\left(u-\frac{\partial u}{\partial x}\frac{\Delta x}{2}-\frac{\partial u}{\partial y}\frac{\Delta y}{2}\right)a_{1x} \\
&\quad+\left(u-\frac{\partial u}{\partial x}\frac{\Delta x}{2}+\frac{\partial u}{\partial y}\frac{\Delta y}{2}\right)a_{3x} \\
&\quad+\left(v-\frac{\partial v}{\partial x}\frac{\Delta x}{2}-\frac{\partial v}{\partial y}\frac{\Delta y}{2}\right)a_{1y} \\
&\quad+\left(v+\frac{\partial v}{\partial x}\frac{\Delta x}{2}-\frac{\partial v}{\partial y}\frac{\Delta y}{2}\right)a_{2y} \\
&\quad-\left(u+\frac{\partial u}{\partial x}\frac{\Delta x}{2}-\frac{\partial u}{\partial y}\frac{\Delta y}{2}\right)a_{2x} \\
&\quad-\left(u+\frac{\partial u}{\partial x}\frac{\Delta x}{2}+\frac{\partial u}{\partial y}\frac{\Delta y}{2}\right)a_{4x} \\
&\quad-\left(v-\frac{\partial v}{\partial x}\frac{\Delta x}{2}+\frac{\partial v}{\partial y}\frac{\Delta y}{2}\right)a_{3y} \\
&\quad-\left(v+\frac{\partial v}{\partial x}\frac{\Delta x}{2}+\frac{\partial v}{\partial y}\frac{\Delta y}{2}\right)a_{4y}=0.
\end{aligned} \tag{2}$$

Assuming that the cross sectional areas in each direction are the same (i.e. $a_{jx} = a_x$, $a_{jy} = a_y$) the above equation simplifies to:

$$\frac{\partial u}{\partial x}a_x\Delta x+\frac{\partial v}{\partial y}a_y\Delta y=0. \tag{3}$$

In order to model groundwater flow (usually considered laminar), the velocity through throats is replaced by the Hagen-Poiseuille law:

$$V_{ij} = \frac{\gamma D_{ij}^2}{32\mu} \frac{h_i - h_j}{l_{ij}}, \tag{4}$$

where D_{ij} is the diameter of the bond connecting the nodes, h_i and h_j are hydraulic heads at nodes (i) and (j), ℓ_{ij} is the length of the bond connecting the nodes, and γ and μ are the specific weight and kinematic viscosity of the fluid, respectively.

Assuming that the length of each pipe (Δx, Δy) is much smaller than the pore network size (L, H), and inserting Eq. (4) into Eq. (3), one gets:

$$\frac{\partial}{\partial x}\left(\frac{\gamma D_x^2}{32\mu}\frac{\partial h}{\partial x}\right) a_x dx + \frac{\partial}{\partial y}\left(\frac{\gamma D_{ij}^2}{32\mu}\frac{\partial h}{\partial y}\right) a_y dy = 0, \tag{5}$$

$$\frac{\partial}{\partial x}\left(\frac{\pi\gamma D_x^4}{128\mu}\frac{\partial h}{\partial x}\right) dx + \frac{\partial}{\partial y}\left(\frac{\pi\gamma D_y^4}{128\mu}\frac{\partial h}{\partial y}\right) dy = 0, \tag{6}$$

$$\frac{\partial}{\partial x}\left(K_x \frac{\partial h}{\partial x}\right) dx + \frac{\partial}{\partial y}\left(K_y \frac{\partial h}{\partial y}\right) dy = 0. \tag{7}$$

Letting $D_x = D_y$, $dx = dy$, and eliminating K:

$$\frac{\partial^2 h}{\partial x^2} + \frac{\partial^2 h}{\partial y^2} = 0. \tag{8}$$

This is the well-known Laplace equation which governs steady state flow in a saturated homogenous porous media.

Now, considering continuity at a typical node (i) surrounded by 4 nodes in a square lattice (Figure 3(a)), the flow equation may be transformed into n-linear equations as:

$$\sum_{j=1}^{4} Q_{ij} = 0, \tag{9}$$

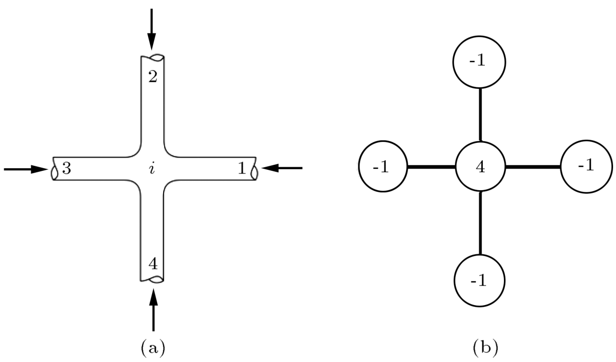

Figure 3. (a) A typical interior node for a Square PNM (SPNM). (b) Computational stencil for the typical node.

$$\sum_{j=1}^{4}\left(\frac{\gamma D_{ij}^2}{32\mu}\frac{h_j - h_i}{L_{ij}}\right)\frac{\pi}{4} D_{ij}^2 = 0, \tag{10}$$

$$\sum_{j=1}^{4} C_{ij}(h_j - h_i) = 0, \tag{11}$$

where:

$$C_{ij} = \frac{\pi\gamma}{128\mu}\frac{D_{ij}^4}{L_{ij}}. \tag{12}$$

For equally spaced nodes (square lattice) connected by pipes with equal cross sectional areas, Eq. (11) yields:

$$4h_i - h_1 - h_2 - h_3 - h_4 = 0. \tag{13}$$

This equation is the equivalent form of discretized Laplace equation and is the same as the central difference formulation for a FD scheme. Eq. (13) holds for each and every interior node in a SPNM. The computational stencil of the equation is shown in Figure 3(b).

2.3. Node connectivity

Node connectivity reflects how a specific node is related or connected to its neighboring nodes. As stated by Raoof and Hassanizadeh [19], in many recent works, nodes are only connected to their neighboring nodes that are located along the lattice axes. This results in no flow along the diagonal direction, even if diagonal pressure gradients exist. In general, one might expect that utilizing more neighboring nodes when discretizing a domain, flow equations would yield more accurate results. Besides concerns of accuracy, if a preferred flow direction is anticipated, it may be advantageous to connect a node to its diagonal neighboring node and/or disconnect it from its certain neighboring node(s).

A typical square diagonal pore network model (S-DPNM), shown in Figure 4, is considered as a PNM with "better" node connectivity. In this model, any interior node is connected to 8 surrounding nodes.

The flow equation for a typical interior node (i), shown in Figure 5(a), may be written as:

$$\left(\sum_{j=1}^{8} C_{ij}\right) h_i - \sum_{j=1}^{8} C_{ij} h_j = 0. \tag{14}$$

The assumption of homogeneity and isotropy drops coefficients C_{ij} out of the above equation. Noticing that diagonal pipe lengths (L_{ij}, j = even) are $\sqrt{2}$ times the lengths of horizontal or vertical pipes (L_{ij}, j = odd), Eq. (14) takes the form of:

$$\left(4 + 4\frac{1}{\sqrt{2}}\right) h_i - \sum_{j=\text{odd}} h_j - \sum_{j=\text{even}} \frac{1}{\sqrt{2}} h_j = 0. \tag{15}$$

The computational stencil for Eq. (15) is shown in Figure 5(b):

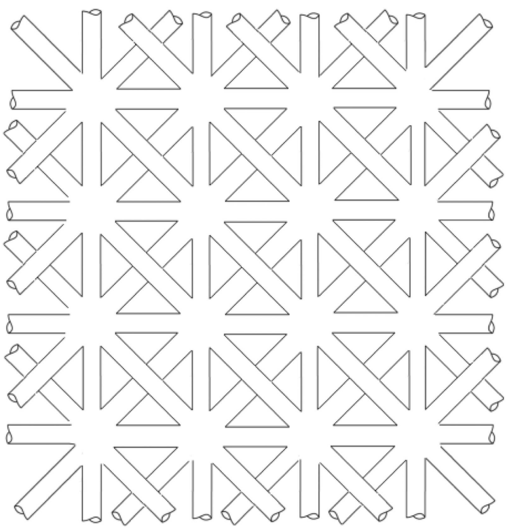

Figure 4. A typical square diagonal pore network model (S-DPNM).

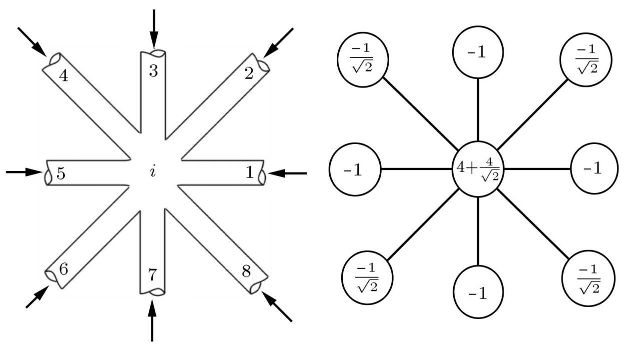

(a) (b)

Figure 5. (a) A typical interior node for the S-DPNM. (b) Computational stencil for the given node.

2.4. Boundary nodes

Two typical boundary nodes (conditions) are considered here:

1. A boundary of prescribed head;
2. An impermeable boundary (no flux).

2.4.1. Prescribed head

This specifies solution values (heads) at the boundary nodes. Application of Eq. (13) is meaningless for these nodes and, therefore, no pipe is needed to connect them. However, pipes are needed to connect the boundary nodes to their adjacent interior nodes. This boundary condition may be written as $h(0, y) = \alpha$ (Figure 6). Applying Eq. (13) to node i yields:

$$4h_i - h_1 - h_2 - h_3 - h_4 = 0,$$

$$4h_i - h_1 - h_2 - h_4 = \alpha, \tag{16}$$

which applies to all interior nodes adjacent to the prescribed head (left) boundary.

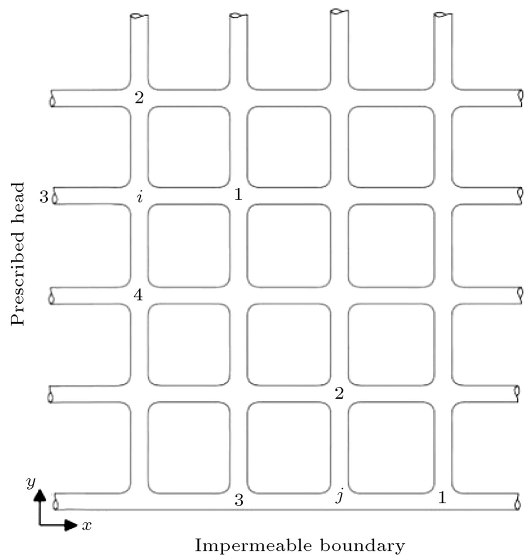

Figure 6. A PNM with specified head nodes at left and impermeable boundary at bottom.

2.4.2. Impermeable boundary

This implies that there is no flow normal to the boundary and may be written as $\frac{\partial h}{\partial n} = 0$, where n is a direction normal to the impermeable boundary. Such nodes may be connected to both interior and adjacent boundary nodes through pipes in a pattern that guarantees no flow into or out of the domain (Figure 6). In such patterns, any flow from interior to boundary nodes would have to bend 90 degrees and flow along the boundary pipe.

For equally spaced nodes connected by pipes with equal cross sectional areas, applying Eq. (11) to a typical boundary node (j) yields:

$$3h_j - h_1 - h_2 - h_3 = 0. \tag{17}$$

Eq. (17) is used for every node lying on the impermeable boundary, and is the same as forward FD formulation for this boundary condition.

Since central FD is more accurate than forward FD in numerical methods [20], numerical modification may be applied to improve the accuracy of impermeable boundary computations in PNMs. To incorporate the accuracy improvement hydraulically, pipe patterns for the boundary nodes may be modified by introducing imaginary nodes below the impermeable boundary (node 4 in Figure 7). Assuming that flow in the imaginary pipe, $4j$, is the same as the flow in pipe $2j$, but in the opposite direction, no total vertical flow at node j is dictated. This assumption may be written as:

$$Q_{j2} = Q_{j4} \rightarrow C_{j2}(h_2 - h_j) = C_{j4}(h_4 - h_j) \rightarrow h_4 = h_2. \tag{18}$$

By replacing h_2 for h_4, Eq. (13) yields:

$$4h_i - h_1 - 2h_2 - h_3 = 0. \tag{19}$$

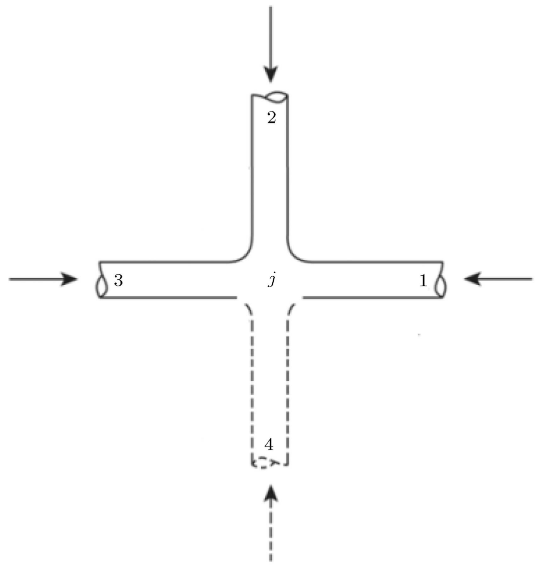

Figure 7. SPNM modification by introducing imaginary node (node 4) located $\triangle y$ beyond the impermeable boundary.

It is worth noting that the above equation is the same as the central difference form for no flux boundaries.

A typical boundary node (i) of an S-DPNM with an impermeable boundary condition at the bottom edge is shown in Figure 8(a).

For pipes with equal cross sectional areas, applying Eq. (15) to node i yields:

$$\left(3+2\frac{1}{\sqrt{2}}\right)h_i-\sum_{j=\text{odd}}h_j-\sum_{j=\text{even}}\frac{1}{\sqrt{2}}h_j=0. \qquad (20)$$

The computational stencil for this equation is shown in Figure 8(b).

The procedure of introducing imaginary nodes/pipes to improve numerical computations may also be done for an S-DPNM in the same manner as SPNM (Figure 9(a)). The no flow boundary condition may be implied by assuming that the flow in corresponding real and imaginary pipes counterbalance one another. In other words:

$$Q_{i6}=Q_{i2}\rightarrow h_6=h_2,$$

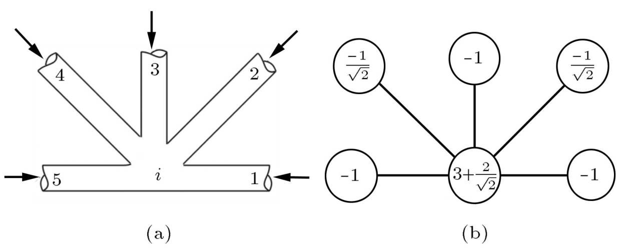

Figure 8. (a) A typical boundary node (i) of an S-DPNM with an impermeable boundary condition at the bottom. (b) Computational stencil for the given node.

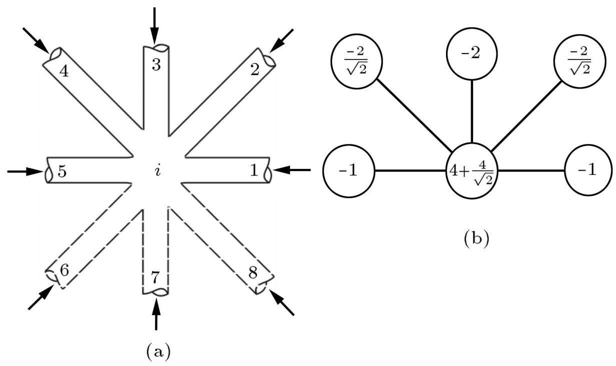

Figure 9. (a) Imaginary nodes/pipes to imply no flow condition at a typical boundary node (i) for an S-DPNM. (b) Computational stencil of the given node.

$$Q_{i7}=Q_{i3}\rightarrow h_7=h_3,$$

$$Q_{i8}=Q_{i4}\rightarrow h_8=h_4. \qquad (21)$$

Using the above results, Eq. (14) may be written as;

$$\left(4+4\frac{1}{\sqrt{2}}\right)h_i-h_1-2h_3-h_5-\frac{2}{\sqrt{2}}h_2-\frac{2}{\sqrt{2}}h_4=0, \qquad (22)$$

whose computational stencil is shown in Figure 9(b).

2.5. General formulation

An advantageous feature of the proposed PNMs is that any number of nodes may be placed at arbitrary locations in the domain connected to other nodes via pipes with any arbitrary pattern. This unstructured node/pipe pattern may be utilized to:

1. Best mimic any anticipated preferred flow direction in the domain;
2. Get more detailed solutions at regions of interest;
3. Better accommodate irregular boundaries.

The general form of Eq. (11) for any typical node (i) surrounded by n nodes (Figure 10(a)) may be written as:

$$\left(\sum_{j=1}^{n}C_{ij}\right)h_i-\sum_{j=1}^{n}C_{ij}h_j=0. \qquad (23)$$

Assigning equal diameters to all connecting pipes results in an isotropic homogenous domain. Eq. (23) reduces to:

$$\left(\sum_{j=1}^{n}\frac{1}{L_{ij}}\right)h_i-\sum_{j=1}^{n}\frac{1}{L_{ij}}h_j=0. \qquad (24)$$

The computational stencil of the above equation for an Unstructured PNM (UPNM) is shown in Figure 10(b).

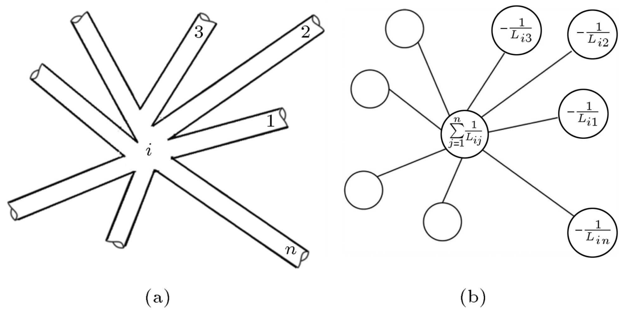

Figure 10. (a) A typical node surrounded by n nodes in an Unstructured PNM (UPNM). (b) Computational stencil of a general UPNM.

By writing Eq. (24) for all unknown nodes of the domain, the algebraic form of the flow equation becomes:

$$[K]\{h\} = \{f\}, \tag{25}$$

where f is the influence of boundary conditions on the domain.

3. Example problems

In order to illustrate the capabilities of the proposed models, three examples are solved. In the first example, steady saturated flow in an isotropic square domain ($L \times L$) is considered (Figure 11). The dimension, L, may be divided into 2, 4 (shown in the figure), 8, 16, 32 and 64 sections. The boundaries, $x = 0$, $x = L$ and $y = L$, are subjected to the Dirichlet boundary conditions of $h = 0$, $h = 0$ and $h = \sin(\frac{\pi x}{L})$, respectively. The boundary $y = 0$ is of a Neumann type, i.e. $\frac{\partial h}{\partial y} = 0$. This example is solved by four models of SPNM, S-DPNM, SPNMi, and S-DPNMi, and the results are compared with analytical ($h = \frac{1}{\cosh(\pi)} \sin\left(\frac{\pi x}{L}\right) \cosh\left(\frac{\pi y}{L}\right)$), as well as linear FE and FD solutions. It is worth noting that the numerical formulation of equations for SPNMi and FD are identical and, hence, only FD results are reported.

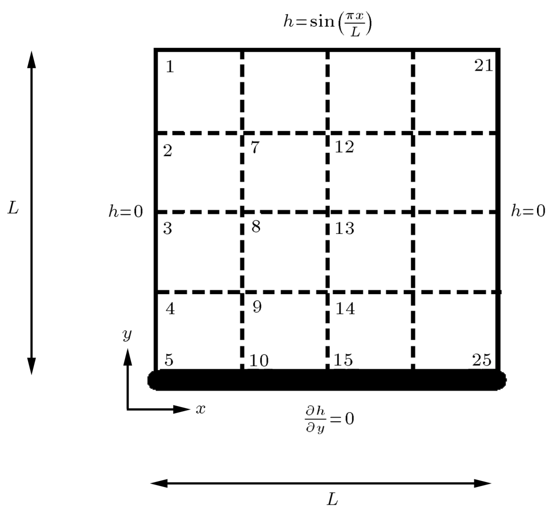

Figure 11. A typical $L \times L$ saturated porous media domain considered as the first example.

Since all pipes have the same length, all C_{ij}s drop out of Eqs. (13) and (17) for SPNM, and one may write these equations for a typical interior node (e.g., node 8) and boundary node (e.g., node 10) as:

$$4h_8 - h_3 - h_7 - h_9 - h_{13} = 0, \tag{26}$$

$$3h_{10} - h_5 - h_9 - h_{15} = 0. \tag{27}$$

Writing Eqs. (26) and (27) for all interior and boundary nodes, respectively, a set of n linear equations is obtained.

In order to solve this example by S-DPNM, Eqs. (15) and (20) may be written for a typical interior node (e.g., node 8) and boundary node (e.g., node 10) as:

$$\left(4 + 4\frac{1}{\sqrt{2}}\right) h_8 - h_3 - h_7 - h_9 - h_{13} - \frac{1}{\sqrt{2}}h_2 - \frac{1}{\sqrt{2}}h_4 - \frac{1}{\sqrt{2}}h_{12} - \frac{1}{\sqrt{2}}h_{14} = 0, \tag{28}$$

$$\left(3 + 2\frac{1}{\sqrt{2}}\right) h_{10} - h_5 - h_9 - h_{15} - \frac{1}{\sqrt{2}}h_4 - \frac{1}{\sqrt{2}}h_{14} = 0. \tag{29}$$

The solution for the example is obtained by applying these equations to relevant nodes.

The example may be solved by S-DPNMi by writing Eqs. (15) and (22) for interior and boundary nodes, respectively:

$$\left(4 + 4\frac{1}{\sqrt{2}}\right) h_8 - h_3 - h_7 - h_9 - h_{13} - \frac{1}{\sqrt{2}}h_2 - \frac{1}{\sqrt{2}}h_4 - \frac{1}{\sqrt{2}}h_{12} - \frac{1}{\sqrt{2}}h_{14} = 0, \tag{30}$$

$$\left(4 + 4\frac{1}{\sqrt{2}}\right) h_{10} - h_5 - 2h_9 - h_{15} - \frac{2}{\sqrt{2}}h_4 - \frac{2}{\sqrt{2}}h_{14} = 0. \tag{31}$$

Head values are computed by the three proposed models, as well as FD and FE, and results are compared with the analytical solution for all nodes. Percent Relative Error (PRE), defined as [20]:

$$\left|\frac{h_{\text{analytical}} - h_{\text{model}}}{h_{\text{analytical}}}\right| \times 100,$$

Table 1. PREs obtained at the center of domain (node 13) by different methods.

No. of Grids	PREs at the center of domain; $x = y = 0.5L$				
	FD	**FE**	**SPNM**	**S-DPNM**	**S-DPNMi**
2×2	31.995	40.389	25.995	30.023	29.312
4×4	8.459	8.951	5.868	7.635	6.728
8×8	2.156	2.187	0.808	2.221	1.653
16×16	0.542	0.544	0.172	0.717	0.412
32×32	0.136	0.136	0.235	0.260	0.103
64×64	0.034	0.034	0.156	0.105	0.026

Table 2. Average PREs for all nodes obtained by different methods.

No. of Grids	Averaged PREs for all nodes				
	FD	**FE**	**SPNM**	**S-DPNM**	**S-DPNMi**
2×2	48.797	51.498	15.688	45.123	38.681
4×4	10.490	10.738	6.571	12.408	8.108
8×8	2.407	2.424	3.099	3.882	1.834
16×16	0.573	0.574	1.736	1.396	0.435
32×32	0.139	0.140	0.952	0.567	0.106
64×64	0.034	0.034	0.474	0.239	0.026

Table 3. max. and min. values of PREs obtained by different methods.

No. of Grids	Max. values of PREs over the entire domain					Min. value of PREs over the entire domain				
	FD	**FE**	**SPNM**	**S-DPNM**	**S-DPNMi**	**FD**	**FE**	**SPNM**	**S-DPNM**	**S-DPNMi**
2×2	65.599	62.607	25.995	60.223	48.050	31.995	40.389	5.381	30.023	29.312
4×4	16.144	16.032	14.323	24.278	12.156	3.995	4.432	2.570	3.468	3.310
8×8	4.025	4.019	12.636	10.292	3.045	0.510	0.527	0.114	0.429	0.397
16×16	1.006	1.005	7.940	4.623	0.761	0.064	0.065	0.009	0.056	0.049
32×32	0.251	0.251	4.416	2.172	0.190	0.008	0.008	0.001	0.008	0.006
64×64	0.063	0.063	2.325	1.000	0.048	0.001	0.001	0.000	0.001	0.001

is computed as an accuracy index for the comparison of results. PREs for head values at the center of the domain (node 13), as a typical node, are reported in Table 1 for different grid sizes. As shown in the table, the general trend is that the error reduces as the number of grids increases for all methods. PRE results for the three models are of the same order or for certain grid sizes smaller, than FD and FE results. In particular, S-DPNMi always shows smaller PREs compared to FD and FE. Quantitatively, results show improvements in PREs of 8% compared to FD, and 27% compared to FE for a 2×2 grid. These improvements approach 24% compared to both methods for grids of 16×16 and higher. Apparently, by introduction of imaginary nodes for the treatment of Neumann type boundaries, much better results may be achieved.

To compare the accuracy of the three models with FD and FE over the entire domain, 1) averaged PREs for all nodes, 2) maximum and minimum PREs, and 3) percentage of nodes with PREs less than that of FD and FE are reported in Tables 2, 3 and 4, respectively. Contour plots of head and velocity vectors are also shown in Figure 12. As shown, plots from all methods are very comparable to the analytical plot. Comparing SPNM vs. S-DPNM in Tables 3 and 4, one may conclude that for fair discretizations, adding diagonal pipes would improve average PREs by lowering their range [min-max]. Apparently, diagonal pipes improve the results by facilitating the spread of information across the domain. Hydraulically speaking, taking into account the diagonal pipes helps better capture the randomness of the pore connections, and results in more accurate fluxes [21]. Introduction of imaginary nodes (S-DPNMi) further improves the averaged PREs and lowers the PREs [min – max] range. Compared to FD and FE, S-DPNMi not only yields better minimum

Table 4. Percent nodes having PREs less than FD and FE using the three proposed models.

Grids	Percent nodes with PREs less than FD			Percent nodes with PREs less than FE		
	SPNM	S-DPNM	S-DPNMi	SPNM	S-DPNM	S-DPNMi
2×2	100	100	100	100	100	100
4×4	100	50	100	100	50	100
8×8	75	37.5	100	75	37.5	100
16×16	56.25	25	100	56.25	25	100
32×32	40.63	6.25	100	40.63	6.25	100
64×64	23.44	0	100	23.44	0	100

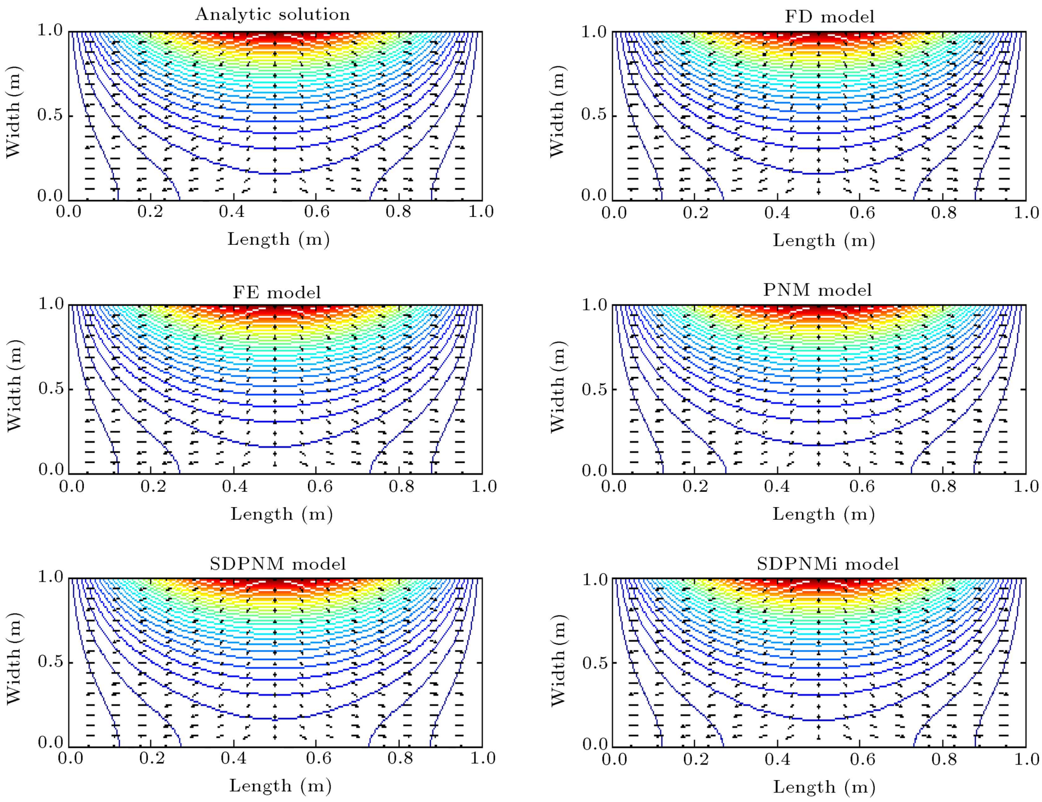

Figure 12. Contour plots of head and velocity vectors using different models.

and maximum PREs, but also lowers the averaged PREs by ∼24%. This superiority for S-DPNMi holds for all grid sizes at all nodes (Table 4).

The fact that in S-DPNMi (unlike FD), diagonal nodes are also considered, increases correlation of the node to its surrounding nodes; something that has apparently caused S-DPNMi to be more accurate than FD. On the other hand, the relations of the node to its surrounding nodes in S-DPNMi are not identical (unlike FE) and depend on the length of bonds. As shown in Figure 6, nodes that are closer to the considered node play a more significant role than those furher away. It seems that this engineered correlation of a node to its surroundings has made S-DPNM more accurate than FE.

The second example considers a steady saturated groundwater flow in a triangular domain, shown in Figure 13. The right boundary is subjected to the Dirichlet condition of $h = \sin(\frac{\pi y}{2L})$, where top and vertices boundaries are impermeable.

Triangular meshes are used to solve this example by FE (Figure 14). However, the given pattern yields identical results for FD and FE. On the other hand, as in the previous example, results for FD and SPNMi would also be the same.

The procedure of solving this example is the same as the previous one, except for the impermeable vertices boundary. Application of SPNM, S-DPNM and S-DPNMi models to a typical node on the vertices boundary (e.g. node 7) yields:

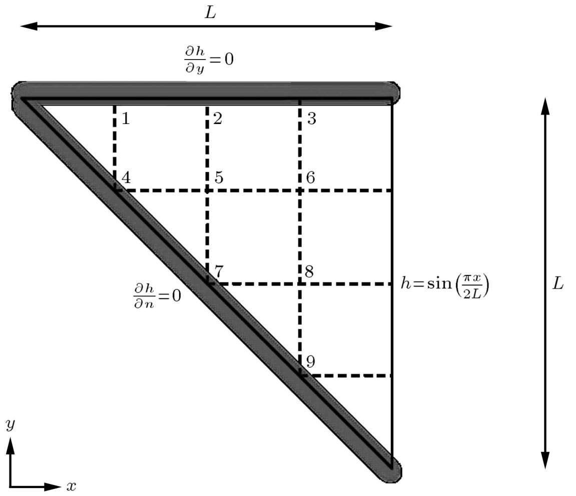

Figure 13. The $L \times L$ triangular domain considered in the second example.

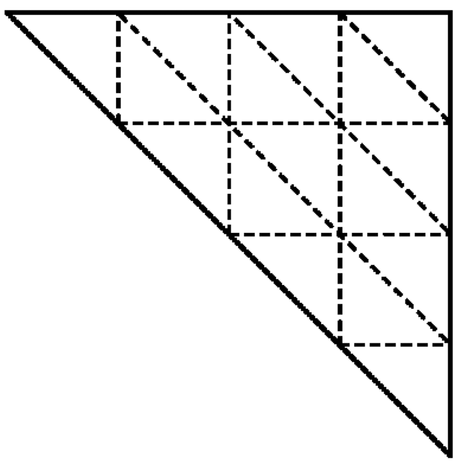

Figure 14. Triangular meshes used to solve the second example by FE.

$$2h_7 - (h_5 + h_8) = 0, \tag{32}$$

$$\left(2 + 3\frac{1}{\sqrt{2}}\right) h_7 - (h_5 + h_8) - \frac{1}{\sqrt{2}}(h_4 + h_6 + h_9) = 0, \tag{33}$$

$$\left(4 + 4\frac{1}{\sqrt{2}}\right) h_7 - (2h_5 + 2h_8) - \frac{1}{\sqrt{2}}(h_4 + 2h_6 + h_9) = 0. \tag{34}$$

By comparing head values obtained by all models with the analytical solution given in the Appendix, PREs for all nodes are calculated. PREs of a typical node (node 7) and the averaged PREs of the entire domain are reported in Tables 5 and 6, respectively. As shown in the tables, the general trend is that the error reduces as the number of grids increases for all methods. Comparing SPNM vs. S-DPNM in Tables 5 and 6, one may conclude that adding diagonal pipes, which results in correlating a node to more of its surrounding nodes, would improve the results. As in the first example, S-DPNMi (introduction of imaginary nodes) always shows smaller PREs compared to FD. Quantitatively, results show improvements in averaged PREs of $\sim 25\%$ compared to FD for all numbers of grids in S-DPNMi.

Table 5. PREs obtained at node 7 by different methods.

No. of Grids	PREs at node 7($x = y = 0.5L$)			
	FD	SPNM	S-DPNM	S-DPNMi
2×2	4.522	7.791	1.365	3.502
4×4	1.174	3.663	0.394	0.896
8×8	0.296	1.779	0.455	0.225
16×16	0.074	0.878	0.293	0.056
32×32	0.019	0.436	0.163	0.019
64×64	0.005	0.218	0.086	0.008

Table 6. Averaged PREs for all nodes obtained by different methods.

No. of Grids	Averaged PREs for all nodes			
	FD	SPNM	S-DPNM	S-DPNMi
2×2	5.609	10.972	0.874	4.057
4×4	1.184	4.501	0.879	0.894
8×8	0.262	1.944	0.578	0.199
16×16	0.061	0.890	0.315	0.046
32×32	0.015	0.424	0.163	0.011
64×64	0.004	0.207	0.082	0.003

Maximum and minimum PREs and percentage of nodes with PREs less than that of FD are also reported in Tables 7, and 8, respectively. As expected, applying the S-DPNMi model yields more accurate results for each and every node with a narrower range of [min − max].

The third example, 2-D potential flow around a cylinder (Figure 15(a)), is too cumbersome to be solved by FD because it cannot easily model boundaries with geometric irregularities. Therefore, the example is solved by FE, and results are compared with UPNM and UPNMi models. The cylinder, as well as bottom and top boundaries, are impermeable, and the left and right boundaries have head values of 20 (m) and 0 (m), respectively. Symmetry exists about the horizontal and vertical centre lines, therefore, only a quadrant of the domain (enclosing 5 unknown nodes) is used as the computational domain (Figure 15(b)).

It should be noted that the computational procedure for UPNM and UPNMi models is much easier than FE because it does not require tedious calculation

Table 7. max. and min. values of PREs obtained by different methods.

No. of Grids	Max. values of PREs over the entire domain				Min. values of PREs over the entire domain			
	FD	SPNM	S-DPNM	S-DPNMi	FD	SPNM	S-DPNM	S-DPNMi
2 × 2	7.086	13.210	1.365	4.447	4.522	7.791	0.029	3.502
4 × 4	1.830	6.597	1.614	1.311	0.590	1.542	0.004	0.455
8 × 8	0.461	3.252	1.095	0.344	0.074	0.305	0.047	0.056
16 × 16	0.116	1.650	0.619	0.087	0.009	0.066	0.018	0.007
32 × 32	0.029	0.833	0.329	0.022	0.001	0.015	0.005	0.001
64 × 64	0.007	0.419	0.170	0.009	0.000	0.004	0.001	0.000

of coefficient matrices for each element and their subsequent assemblage. To show the procedure of solving this example by UPNM, Eq. (24) is applied to a typical node (node 2):

Table 8. Percent nodes having PREs less than FD using the three proposed models.

Grids	Percent nodes with PREs less than FD		
	SPNM	S-DPNM	S-DPNMi
2 × 2	0	75	100
4 × 4	0	2	100
8 × 8	0	0	100
16 × 16	0	0	100
32 × 32	0	0	100
64 × 64	0	0	100

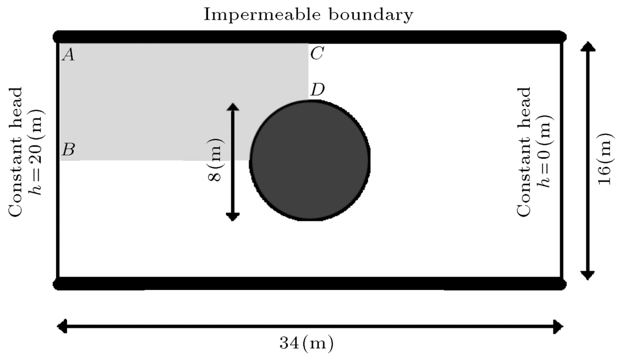

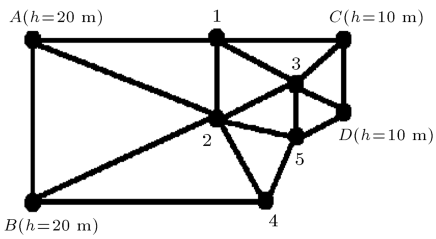

Figure 15. (a) Potential flow around a cylinder. (b) Discretized quadrant (shaded area in Figure 12(a)) as the computational domain.

$$1.09h_2 - 0.09h_a - 0.09h_b - 0.25h_1 - 0.23h_3 - 0.2h_4 - 0.23h_5 = 0, \tag{35}$$

where head coefficients (reciprocal pipe lengths connecting to node 2) are obtained from Table 9. Applying Eq. (24) to other nodes and replacing h_a, h_b, h_c and h_d by their known values, one would get a system of 5 linear equations with 5 unknowns. Application of UPNMi requires some amendment to impermeable boundary node formulations. As an example, to treat node 5, two imaginary pipes 52i and 53i should be introduced to counterbalance the flow in pipes 52 and 53. A computational stencil for node 5 is shown in Figure 16.

Head values for all 5 nodes are obtained using UPNM, UPNMi, and linear FE. Comparing the heads with the analytical solution, PREs are calculated and reported in Table 10. The analytical solution may be found as [21]:

$$h = Ur\left(1 + \frac{a^2}{r^2}\right)\cos\theta,$$

where h is the head, a is the radius of the cylinder, r and θ are coordinates of any point in the domain, and U is the uniform stream velocity. As shown, using UPNM yields smaller PREs compared to FE for most nodes. As expected, application of imaginary nodes (UPNMi) further improves the results, as evidenced by much smaller PREs than FE for all nodes. Averaged

Table 9. Lengths of pipes connecting to node 2 and head coefficients for that node.

Pipe	$L_{ij}\,(m)$	$\frac{1}{L_{ij}}\ (\frac{1}{m})$	$\sum_{j=1}^{n} \frac{1}{L_{ij}}\ (\frac{1}{m})$
2a	10.77	0.09	
2b	10.77	0.09	
21	4.00	0.25	
23	4.43	0.23	
24	5.00	0.20	
25	4.33	0.23	1.09

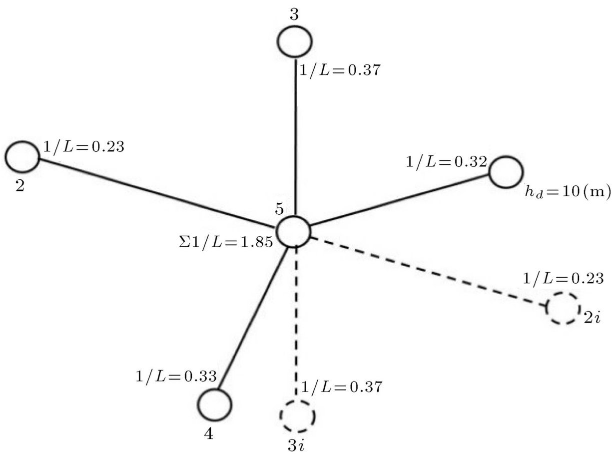

Figure 16. Computational stencil for node 5 using UPNMi.

Table 10. PREs obtained by UPNM, UPNMi and FE for all five nodes and their average.

Nodes	PREs		
	FE	**UPNM**	**UPNMi**
1	11.004	7.687	6.344
2	28.962	6.133	3.693
3	14.086	4.229	2.443
4	18.994	4.870	1.600
5	5.238	7.754	4.092
Averaged PREs	15.657	6.135	3.634

PREs for UPNM and UPNMi are 0.4 and 0.23 of PREs for FE. It may be concluded that computational procedures for UPNM and UPNMi models are not only much easier than FE, but also yield much more accurate results.

4. Conclusion

The Square Pore Network Model (SPNM) was introduced, investigated and used to solve steady saturated flow in porous media. By applying the continuity equation and using the Hagen-Poiseuille law, a discretized form of the flow equation was derived. Modifications for the model were done by 1) increasing node connectivity (Square Diagonal PNM; S-DPNM) in order to have a better spread of information across the domain, and 2) introducing imaginary nodes and pipes (S-DPNMi) to model impermeable boundaries. Furthermore, an Unstructured Pore Network Model (UPNM), as a generalized formulation for unstructured discretization of the domain, was given and the effects of introducing imaginary nodes and pipes in the model were also explored (UPNMi). Applying SPNM, S-DPNM, and S-DPNMi to the first and second examples yielded average Percent Relative Errors (PREs) that were comparable to those of FD and FE for the first two models and smaller for the third. It was concluded that modification in handling impermeable boundaries by the introduction of imaginary nodes and pipes and by increasing node connectivity would improve results considerably. In fact, improvements in PREs of 8% compared to FD and 27% compared to FE for a 2×2 grid were achieved for the first example. These improvements approached 24% compared to both methods for grids of 16×16 and higher. This improvement was ∼25% for all numbers of grids in the second example. In the third example, which was too cumbersome to be solved by finite difference, UPNM and UPNMi application resulted in the average PREs of 0.4 and 0.23 of PREs obtained by FE, respectively. As before, modification in handling impermeable boundaries improved the results of the unstructured model. It was concluded that using PNM as a numerical tool to solve steady saturated flow in porous media not only simplifies the modeling formulation compared to FD and FE, but also may yield more accurate results. Applicability of the models is limited to Partial Differential Equations (PDEs) having spatial derivatives of the form ∇_u^2; steady saturated groundwater flow being one of them. Luckily, spatial derivatives in many PDEs in engineering and science problems, such as wave, heat, Laplace, Poisson, and Helmholtz equations, are of this form.

References

1. Piri, M. and Blunt, M.J. "Three-dimensional mixed-wet random pore-scale network modeling of two-and three-phase flow in porous media. I. Model description", *Physical Review E.*, **71** (026301), pp. 1-30 (2005).

2. Al-Raoush, R.I. and Willson, C.S. "A pore-scale investigation of a multiphase porous media system", *Journal of Contaminant Hydrology*, **77**, pp. 67-89 (2005).

3. Ioannidis, M.A. and Chatzis, I. "Network modeling of pore structure and transport properties of porous media", *Chemical Engineering Science*, **48**, pp. 951-972 (1993).

4. Man, H.N. and Jing, X.D. "Pore network modelling of electrical resistivity and capillary pressure characteristics", *Transport in Porous Media*, **41**, pp. 263-286 (2000).

5. Joekar-Niasar, V., Prodanovic, M., Wildenschild, D. and Hassanizadeh, S.M. "Network model investigation of interfacial area, capillary pressure and saturation relationships in granular porous media", *Water Resources Research*, **46** (W06526, doi:10.1029/2009WR008585), pp. 1-18 (2010).

6. Joekar-Niasar, V., Hassanizadeh, S.M., Pyrak-Nolte, L. and Berentsen, C. "Simulating drainage and imbibition experiments in a high-porosity micromodel using an unstructured pore network model", *Water Resources Research*, **45** (W02430 doi:10.1029/2007WR006641), pp. 1-15 (2009).
7. Joekar-Niasar, V., Hassanizadeh, and S.M. Leijnse, A. "Insights into the relationships among capillary pressure, saturation, interfacial area and relative permeability using pore-network modeling", *Transport in Porous Media*, **74**, pp. 201-219 (2008).
8. Thauvin, F. and Mohanty, K.K. "Network modeling of non-Darcy flow through porous media", *Transport in Porous Media*, **31**, pp. 19-37 (1998).
9. Tsakiroglou, C.D. and Payatakes, A.C. "Characterization of the pore structure of reservoir rocks with the aid of serial sectioning analysis, mercury porosimetry and network simulation", *Advances in Water Resources*, **23**, pp. 773-789 (2000).
10. Acharya, R.C., van der Zee, S.E.A.T.M. and Leijnse, A. "Porosity-permeability properties generated with a new 2-parameter 3D hydraulic pore-network model for consolidated and unconsolidated porous media", Advances in Water Resources, **27**, pp. 707-723 (2004).
11. Nsir, K. and Schafer, G. "A pore-throat model based on grain-size distribution to quantify gravity-dominated DNAPL instabilities in a water-saturated homogeneous porous medium", *Comptes Rendus Geoscience*, **342**, pp. 881-891 (2010).
12. Steele, D.D. and Nieber, J.L. "Network modeling of diffusion coefficients for porous media: II simulations", *Soil Science Society of American Journals*, **58**, pp. 1346-1354 (1994).
13. Fatt, I. "The network model of porous media I. Capillary pressure characteristics", *Transactions American Institute of Mining, Metallurgical, and Petroleum Engineers*, **207**, pp. 144-159 (1956).
14. Koplic, J. "Creeping flow in two-dimensional networks", *Journal of Fluid Mechanics*, **119**, pp. 219-247 (1982).
15. Mazaheri, A.R., Zerai, B., Ahmadi, G., Kadambi, J.R., Saylor, B.Z., Oliver, M., Bromhal, G.S. and Smith, D.H. "Computer simulation of flow through a lattice flow-cell model", *Advances in Water Resources*, **28**, pp. 1267-1279 (2005).
16. Øren, P.E., Bakke, S. and Arntzen, O.J. "Extending predictive capabilities to network models", *Society of Petroleum Engineers Journals*, **3**, pp. 324-336 (1998).
17. Kagan, M. and Pinczewski, W.V. "Menisci in a diamond-shaped capillary", *Journal of Colloid Interface Science*, **230**, pp. 452-454 (2000).
18. Dias, M.M. and Payatakes, A.C. "Network models for two-phase flow in porous media. Part 1. Immiscible microdisplacement of non-wetting fluids", *Journal of Fluid Mechanics*, **164**, pp. 305-336 (1985).
19. Raoof, A. and Hassanizadeh, S.M. "A new method for generating pore-network models of porous media", *Transport in Porous Media*, **8**, pp. 391-407 (2010).
20. Chapra, S.C. and Canale, P.C., *Numerical Methods for Engineers*, 6th Ed., McGraw-Hill (2009).
21. Munson, B.R., Young, D.F., Okiishi, T.H. and Huebsch, W.W., *Fundamental of Fluid Mechanics*, 6th Ed., John Wiley & Sons, Inc (2009).

Appendix

To solve the second example analytically. the Laplace equation was solved for the given boundaries in an $L\times L$ square domain, shown in Figure A.1(a). The solution was found using the separation of variables technique:

$$h=\frac{1}{\cosh\left(\frac{\pi}{L}\right)}\cosh\left(\frac{\pi x}{2L}\right)\sin\left(\frac{\pi y}{2L}\right). \tag{A.1}$$

By rotating the domain around diagonal AB, as shown in Figure A.1(b), one would get the solution using the above equation by replacing y with x, and x with $L-y$:

$$h=\frac{1}{\cosh\left(\frac{\pi}{L}\right)}\cosh\left(\frac{\pi(L-y)}{2L}\right)\sin\left(\frac{\pi x}{2L}\right). \tag{A.2}$$

Using the superposition principle, the solution of the Laplace equation for the domain shown in Figure A.1(c) is found as:

$$\begin{aligned}h=&\frac{1}{\cosh\left(\frac{\pi}{2L}\right)}\left\{\cosh\left(\frac{\pi x}{2L}\right)\sin\left(\frac{\pi y}{2L}\right)\right.\\&\left.+\sin\left(\frac{\pi x}{2L}\right)\cosh\left(\frac{\pi(L-y)}{2L}\right)\right\}.\end{aligned} \tag{A.3}$$

It will be shown mathematically that Eq. (A.3) has no flux across the diagonal AB. In other words, Eq. (A.3) is shown to be the solution of the triangular domain in the second example. Consider an L translation for y, and a 45° rotation for the $X-Y$ coordinate system (Figure A.2). Then, Eq. (A.3) in the $X-Y$ coordinate system would be:

$$\begin{aligned}h=&\frac{1}{\cosh\left(\frac{\pi}{2L}\right)}\left\{\cosh\left(\frac{\pi X}{2L}\right)\sin\left(\frac{\pi(L+Y)}{2L}\right)\right.\\&\left.+\sin\left(\frac{\pi X}{2L}\right)\cosh\left(\frac{\pi Y}{2L}\right)\right\}.\end{aligned} \tag{A.4}$$

To find the solution in the $\xi-\eta$ system, the 45° rotational matrix is used:

$$\begin{Bmatrix}X\\Y\end{Bmatrix}=\begin{bmatrix}\cos(45)&\sin(45)\\\sin(45)&\cos(45)\end{bmatrix}\begin{Bmatrix}\xi\\\eta\end{Bmatrix}. \tag{A.5}$$

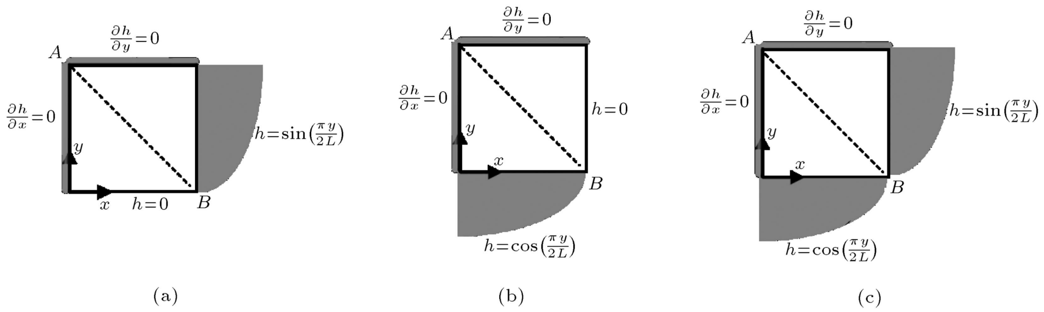

Figure A.1. (a) An $L \times L$ square domain. (b) Rotated around diagonal AB. (c) Superposition of (a) and (b).

Inserting the above transformation into Eq. (A.4) yields:

$$h = \frac{1}{\cosh\left(\frac{\pi}{2L}\right)} \left\{\cosh\left(\frac{\pi}{2L}\left(\frac{\sqrt{2}}{2}\xi + \frac{\sqrt{2}}{2}\eta\right)\right) \sin\left(\frac{\pi}{2L}\left(L - \frac{\sqrt{2}}{2}\xi + \frac{\sqrt{2}}{2}\eta\right)\right) + \sin\left(\frac{\pi}{2L}\left(\frac{\sqrt{2}}{2}\xi + \frac{\sqrt{2}}{2}\eta\right)\right) \cosh\left(\frac{\pi}{2L}\left(-\frac{\sqrt{2}}{2}\xi + \frac{\sqrt{2}}{2}\eta\right)\right)\right\}. \tag{A.6}$$

Differentiating the above equation with respect to η, and setting η=0 results in:

$$\left.\frac{\partial h}{\partial \eta}\right|_{\eta=0} = \frac{\pi}{2L}\frac{\sqrt{2}}{2\cosh\left(\frac{\pi}{2L}\right)} \left\{\sinh\left(\frac{\sqrt{2}\pi}{4L}\xi\right)\sin\left(\frac{\pi}{2L}\left(L - \frac{\sqrt{2}}{2}\xi\right)\right) + \cosh\left(\frac{\sqrt{2}\pi}{4L}\xi\right)\cos\left(\frac{\pi}{2L}\left(L - \frac{\sqrt{2}}{2}\xi\right)\right) + \cos\left(\frac{\sqrt{2}\pi}{4L}\xi\right)\cosh\left(\frac{\sqrt{2}\pi}{4L}\xi\right) - \sin\left(\frac{\sqrt{2}\pi}{4L}\xi\right)\sinh\left(\frac{\sqrt{2}\pi}{4L}\xi\right)\right\}, \tag{A.7}$$

which simplifies into:

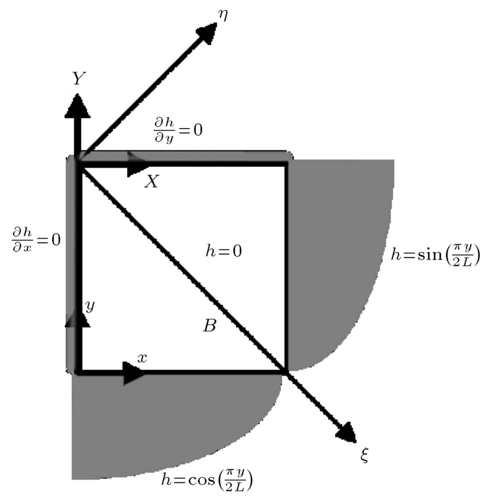

Figure A.2. Different coordination for the considered problem.

$$\left.\frac{\partial h}{\partial \eta}\right|_{\eta=0} = \frac{\pi}{2L}\frac{\sqrt{2}}{2\cosh\left(\frac{\pi}{2L}\right)} \left\{\sinh\left(\frac{\sqrt{2}\pi}{4L}\xi\right)\left[\sin\left(\frac{\pi}{2L}\left(L - \frac{\sqrt{2}}{2}\xi\right)\right) - \sin\left(\frac{\sqrt{2}\pi}{4L}\xi\right)\right] + \cosh\left(\frac{\sqrt{2}\pi}{4L}\xi\right)\left[\cos\left(\frac{\pi}{2L}\left(L - \frac{\sqrt{2}}{2}\xi\right)\right) + \cos\left(\frac{\sqrt{2}\pi}{4L}\xi\right)\right]\right\}. \tag{A.8}$$

By expanding:

$$\sin\left(\frac{\pi}{2L}\left(1 - \frac{\sqrt{2}}{2}\xi\right)\right),$$

and:

$$\cos\left(\frac{\pi}{2L}\left(1-\frac{\sqrt{2}}{2}\xi\right)\right),$$

the arguments in the two brackets in Eq. (A.8) turn into zero, resulting $\frac{\partial h}{\partial \eta}=0$.

Biographies

Parjang Monajemi received his BS, MS, and Ph.D. degrees in Environmental Engineering, in 2002, 2005 and 20013, respectively, from Shiraz University, Iran. His research interests include: biological wastewater treatment, and mathematical modeling in environmental engineering

Reza Rakhshandehroo received his BS degree from Shiraz University in 1985, and MS and PhD degrees from Michigan State University, USA. He is currently Professor in the Civil Engineering Department at Shiraz University, Iran, and Vice Chancellor of Student Affairs. His research interests include: water resources engineering, specializing in groundwater hydraulic and contaminant transport.